ARTICLE NO. 78-1337R

Symmetric Body Vortex Wake Characteristics in Supersonic Flow

William L. Oberkampf* and Timothy J. Bartel†
The University of Texas at Austin, Austin, Texas

An extensive experimental investigation of the symmetric body vortex wake was conducted. Cone probe measurements were made on the leeside of an ogive nose circular cylinder for three different supersonic freestream conditions. Measurements of total pressure, Mach number, and three orthogonal velocity components were made at four angles of attack of the body at various axial stations. In the present paper, these data are processed to infer the position of the primary-body vortex and vortex feeding sheet in the cross-flow plane, local circulation distribution in the cross-flow plane, vortex core size, wake height, and total circulation in the cross-flow plane. A detailed discussion of the results and data processing is presented.

Nomenclature

d	= body diameter
h	= circulation contour size (square $h \times h$, $h = 0.0375\,d$)
M	= Mach number
p_0	= total pressure (upstream of probe normal shock)
R_d	= Reynolds number based on body diameter
r_z, r_y	= vortex radii in (r', ϕ) axis system
r^1, ϕ	= polar coordinates in vortex orientated axis system
u, v, w	= velocity components in body axis system (Fig. 2)
U_c	= magnitude of cross-flow velocity $(\sqrt{v^2 + w^2})$
U_∞, U_i	= freestream speed
x, y, z	= body coordinate system (Fig. 2)
y_v, z_v	= primary vortex center location in body axis system
z_s	= secondary nose vortex height in body axis system
z_w	= wake height
α_b	= angle of attack of the body
Γ	= local circulation in cross-flow plane (contour $h \times h$)
Γ_t	= total circulation in survey grid
Ψ	= stream function

Subscript

∞	= freestream conditions

I. Introduction

HIGH-angle-of-attack aerodynamics has become an increasingly important topic in atmospheric flight mechanics. Nonlinear forces and moments which come into existence at high incidence angles have caused a number of flight stability and controlability problems on both missiles and aircraft. Many of the nonlinear forces and moments produced by a body or attached lifting surfaces are caused by the existence of the vortex wake on the leeside of the body. At angles of attack above about 10 deg symmetric vortices form on the leeside of the body and grow in strength along the body. If the angle of attack or body length is increased, the symmetric wake develops along the body into an asymmetric multiple vortex wake. The present investigation is concerned with the symmetric body vortex wake in supersonic flow.

Presented as Paper 78-1337 at the AIAA Atmospheric Flight Mechanics Conference; submitted Sept. 1, 1978; revision received April 17, 1980.

Index categories: Supersonic and Hypersonic Flow; Jets, Wakes, and Viscid-Inviscid Flow Interactions; LV/M Aerodynamics.

*Associate Professor, Mechanical Engineering Dept. (presently, Member of the Technical Staff, Sandia National Laboratories, Albuquerque, N. Mex.). Associate Fellow AIAA.

†Graduate Student, Mechanical Engineering Dept. (presently, Member of the Technical Staff, Sandia National Laboratories, Albuquerque, N. Mex.).

The early experimental work in body vortex flowfield measurements was conducted by Jorgensen and Perkins.[1] They conducted pitot pressure surveys and a limited number of downwash velocity measurements in supersonic flow. More complete supersonic flowfield measurements of the symmetric wake were made by Mello.[2] Total pressure surveys and cross-flow velocity measurements were made using a conical pressure probe. More recently, Thomson and Morrison[3] conducted an extensive experimental investigation of the asymmetric vortex wake of a cone cylinder. They made pitot pressure, cross-flow velocity, and Schlieren photographic measurements for several supersonic Mach numbers and body stations.

The present paper describes the most comprehensive experimental investigation to date of the symmetric body vortex wake of a circular cylinder body in supersonic flow. Total pressure, Mach number, and three orthogonal velocity components were measured at various survey planes on the leeside of the body. Measurements were made at a nominal Mach number of 2 for two Reynolds numbers and at Mach 3 for one Reynolds number. The high Reynolds number condition ($R_d = 1.75 \times 10^6$) represents a factor of four increase over previously published data for supersonic flow. The measurements were made using a conical pressure probe which was manipulated by computer in angular orientation and position in the wind tunnel. The first paper documenting this investigation[4] describes in detail the experimental technique and presents results for basic flowfield data: total pressure, Mach number, and three-dimensional velocity components. This paper concentrates on presenting important results from implied data, e.g., vortex centers and circulation distribution. Complete reporting of the experiment and results is given in Ref. 5.

II. Experimental Investigation

The experimental program was conducted in Supersonic Tunnel A of the von Kármán Gas Dynamics Facility of the Arnold Engineering Development Center, Arnold Air Force Station, Tenn. Tunnel A is a continuous-flow, closed-circuit wind tunnel with a 1.02×1.02 m (40×40 in.) test section. The model used in this experiment was a 76.2 mm (3 in.) diameter circular cylinder with a two-caliber tangent ogive nose and a total length of 1.143 m (45 in.). It was supported by a sting and strut assembly. The wake flow measurements were made with a biconic shaped pressure probe with a diameter of 3.17 mm (0.125 in.) at the union of the two cones and a 20 deg semiapex angle of the tip cone. The probe was constructed with four static pressure orifices on the cone surface and a total pressure orifice at the apex of the cone. The probe was supported by a double-offset, wedge-shaped strut mounted on the captive trajectory system (CTS) of the wind tunnel. A

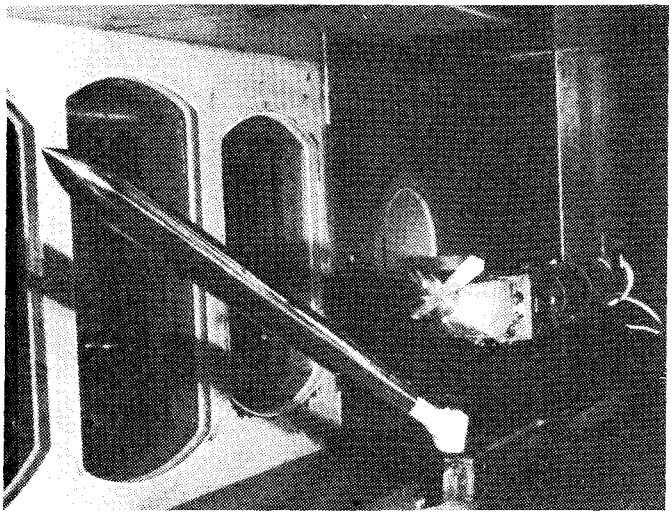

Fig. 1 Wind tunnel installation.

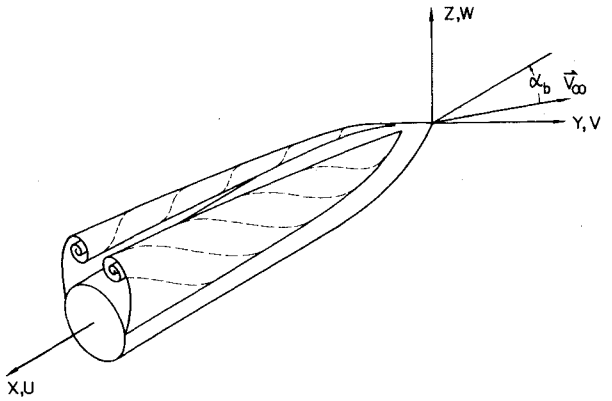

Fig. 2 Coordinate system.

photograph of the model and probe installation is shown in Fig. 1.

The CTS is a computer-controlled electromechanical drive system permitting variation of all six degrees of freedom. The CTS, originally designed for simulations of store separation from a parent body in the wind tunnel, was used as a probe-manipulating mechanism in a new experimental technique. During the flowfield probing phase, the CTS was programmed to position the probe at the series of grid points in the cross-flow plane, i.e., the y-z plane shown in Fig. 2. Data were taken in the right-half cross-flow plane as the axial body stations were chosen such that the vortex wake would be symmetric at the survey locations. Two or three axially located grids were surveyed, depending on the angle of attack, with grid point spacing of 5.72 mm (0.225 in.). A summary of wind-tunnel freestream conditions, model angles of attack, and axial grid locations is shown in Table 1. The final data set totaled 5341 survey points evenly distributed at the three freestream conditions. At each survey point five flow parameters were obtained: total pressure, Mach number, and three velocity components.

Each grid was divided into subgrids where constant probe orientation angles were specified. Each subgrid contained 1-14 grid points. The particular angles within a subgrid were chosen using computer-generated results from the flowfield model discussed in Refs. 6 and 7. The probe angles and size of the subgrids were chosen so that the angle between the probe axis and the local velocity was minimized.

During the experiment a new type of computer/wind tunnel interaction was employed to allow real time analysis of the data. Immediately after a grid was surveyed, local flow parameters, angle of attack of the probe, and the local flow

Table 1 Flowfield survey conditions

M_∞	U_∞, m/s	$R_d \times 10^{-6}$	α_b, deg	x/d
2.00	514	1.75	10	8, 11, 14
2.00	514	1.75	15	7, 10, 13
2.00	514	1.75	20	6, 8.5, 11
2.00	514	1.75	25	6, 9
1.95	549	0.48	10	8, 11, 14
1.95	549	0.48	15	7, 10, 13
1.95	549	0.48	20	6, 8.5, 11
1.95	549	0.48	25	6, 9
3.01	645	1.70	10	8, 11, 14
3.01	645	1.70	15	7, 10, 13
3.01	645	1.70	20	6, 8.5, 11
3.01	645	1.70	25	6, 9

circulation in the cross-flow plane were calculated. The data were then scanned and the CTS computer immediately reprogrammed either to reduce the angle of attack of the probe or to increase or decrease the survey region size as necessary. The initial probe angle estimates were generally very good and only a small percentage of the initial survey points were repeated because of large probe angles of attack. The average angle of attack of the probe for the final data set was 8.2 deg.

III. Results and Discussion

Characteristics of Vortex Wake

The characteristics of the symmetric body vortex wake for freestream Mach number of 1.95 and Reynolds number (based on diameter) of 0.48×10^6 will be discussed in this section. This freestream condition corresponds closely to the previously published data of Jorgensen and Perkins[1] and Mello.[2] Results for $M_\infty = 2.00$ and $R_d = 1.75 \times 10^6$ and for $M_\infty = 3.01$ and $R_d = 1.70 \times 10^6$ will be given in the next subsections. The present paper discusses results which are numerically processed from the basic flow quantities of total pressure, Mach number, and three-dimensional velocity components. As the numerical processing techniques are central to the computation and interpretation of the data, a summary of these procedures will be discussed. For a complete description of the data processing and presentation of the experimental results from this investigation, see Ref. 5.

Probably the most important parameter of the body vortex is its location in the cross-flow plane. Not only is it an important and difficult parameter for theoretical techniques to predict, but it is also a crucial element in order to determine the load distribution imposed on a wing or fin immersed in this flow. The primary vortex location was determined in the present investigation by analyzing the variation of total pressure, $p_0/p_{0\infty}$, and magnitude of cross-flow velocity, U_c/U_∞ where $U_c = \sqrt{v^2 + w^2}$, in the cross-flow plane. In each of the cross-flow planes measured, contour line plots of $p_0/p_{0\infty}$ and U_c/U_∞ were generated and plotted. A two-dimensional quadratic interpolation scheme was used for the data in the cross-flow plane in order to generate the contours.

In the core of the body vortex the total pressure and the magnitude of the cross-flow velocity decrease because of the "solid body" type of rotational motion. At the center of the core the total pressure and cross-flow velocity attain a local minimum. On contour plots of these parameters the core region appears as closed contours, with the location of the minimum contour denoting the vortex center. For angles of attack of 10 and 15 deg the location of the contour minimum for both total pressure and cross-flow velocity were nearly coincidental. For $\alpha_b = 20$ and 25 deg the contours of cross-flow velocity tended to become very elongated in the z direction, that is, $\partial U_c/\partial z \simeq 0$ along a line $z =$ constant passing through the vortex center. For these cases the total pressure contours yielded a better means of determining vortex centers.

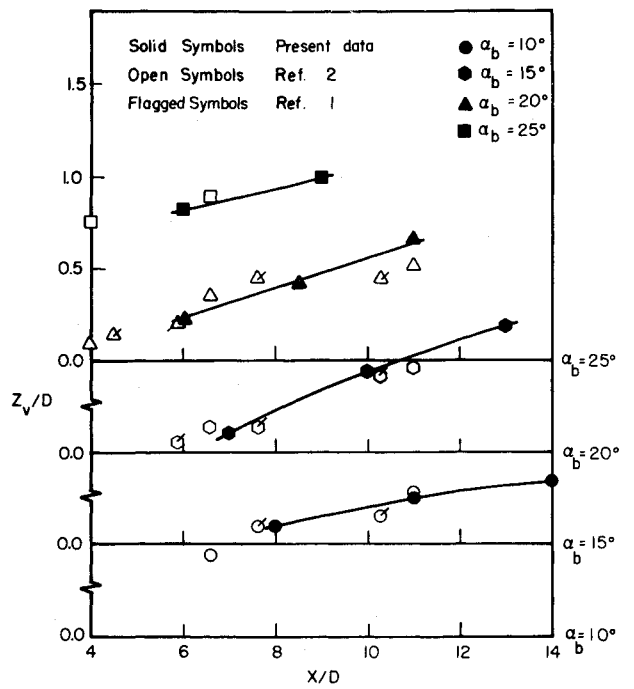

a) z_v/d vs x/d

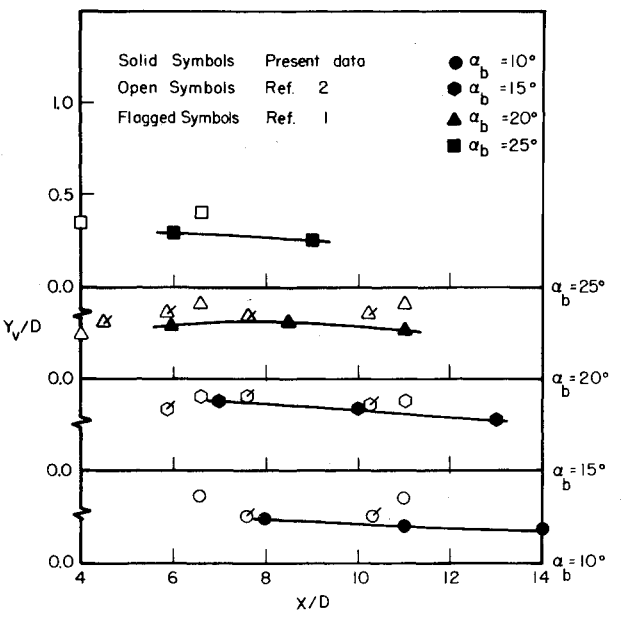

b) y_v/d vs x/d

Fig. 3 Vortex center location in cross-flow plane for $M_\infty = 1.95$ and $R_d = 0.48 \times 10^6$.

Figure 3 shows the measured vortex centers in the cross-flow plane vs x/d for $\alpha_b = 10$, 15, 20, and 25 deg. In order to be able to interpret all of the data on one graph the ordinate for each angle of attack is displaced by $0.5d$. As can be seen from Fig. 3, the y and z coordinates of the body vortex vary linearly over the axial stations measured. The vortex path down the body is essentially in a plane which is slightly tilted toward the z axis. The present data compare closely with the previous data of Jorgensen and Perkins[1] and Mello,[2] even though the nose shapes of each model were different. Jorgensen and Perkins used a three-caliber tangent ogive nose and Mello used a 15 deg half-angle cone. Two slight differences in the three data sets are evident. First, z_v/d data (Fig. 3a) at $\alpha_b = 20$ deg for Jorgensen and Perkins and Mello indicate that a constant value is attained near $x/d = 10$. Certain Schlieren photographs of Thomson and Morrison[3] suggest that the vortices maintain a nearly constant z height shortly before they "break away" into the asymmetric wake pattern. The earlier development of the asymmetric wake along the body would be expected with the models of Jorgensen and Perkins and Mello because of their sharper nose. Second, the y_v/d data (Fig. 3b) of Mello show that the vortex of the cone cylinder is located slightly farther from the angle-of-attack plane, i.e., the x,z plane.

Using the cross-flow velocity data $V_c = vj + wk$, the local circulation was calculated in each of the cross-flow survey planes. The distribution of local circulation $\Gamma(y,z)$ in the cross-flow plane provides significantly more insight to the fluid dynamics of the separated flow as compared to total circulation calculations of previous investigators. In order to compute successfully $\Gamma(y,z)$, assuming two-dimensional (2-D) flow in the cross-flow plane, several numerical procedures were necessary. First, 2-D surfaces were numerically generated for v and w in the cross-flow plane. A 2-D cubic spline computer program was employed and a fitting option utilized so as to avoid regions without data, e.g., the quadrant of the body. The extent of smoothing, however, was minimized and the generated surfaces are essentially interpolated surfaces. With the surfaces determined, function values and first and second derivatives could be evaluated at any point in the region. Approximately 300 s of CDC 6600 time were required to generate the basis function representation of the two velocity surfaces for an average sized grid.

Local circulation was calculated on a square with side $h = 0.0375\ d$, i.e., one-half of the survey grid size. Using the definition of circulation, one has

$$\Gamma \equiv \oint_R V \cdot ds = \int_{y,z}^{y+h,z} v\,dy - \int_{y,z+h}^{y+h,z+h} v\,dy + \int_{y+h,z}^{y+h,z+h} w\,dz - \int_{y,z}^{y,z+h} w\,dz$$

where Γ is positive counterclockwise. A cubic polynomial approximation was used to carry out the numerical integration indicated above. This technique yielded significantly improved results compared to linear approximation because of very large gradients in velocity near the vortex sheet.

A perspective plot of the local circulation $\Gamma(y,z)$ for $\alpha_b = 15$ deg and $x/d = 7$, 10, and 13 is shown in Fig. 4. The perspective view is from above a three-dimensional surface of $\Gamma(y,z)$ and looking in the positive y and negative z directions. The positive y and positive z quadrant of the body can be seen inside the arc of the body surface bounded by the coordinate axes. The "blank" portion near the body surface represents the region where data were not obtained. Lines hidden from the viewer are plotted as dashed lines. The surface of the perspective plot is numerically constructed by connecting the measured data points with straight lines. The quadrant of the body and the coordinate system are displaced from the survey grid by 0.01875 d, that is, one-half of the circulation contour size. The circulation value at the intersection of straight lines on the surface is that value associated with a square of 0.0375 d on a side centered on the surface point.

From Fig. 4a it can be seen that a very concentrated vortex has formed just above the lee surface of the body. The vortex sheet can be seen as a narrow ridge extending from the crest of the body into a peak of vorticity in the vortex core; outside of the core and the sheet, the vorticity is uniformly zero. At $x/d = 10$ (Fig. 4b) the highly concentrated vorticity of the vortex core and sheet has begun to diffuse due to the action of viscosity. At $x/d = 13$ (Fig. 4c) the vorticity has spread over a larger region of the cross-flow plane. Note that the concentration of vorticity along the sheet is nearly constant near the body and then drops off rapidly just before it enters the core. Considering the two-dimensional impulse flow analogy,

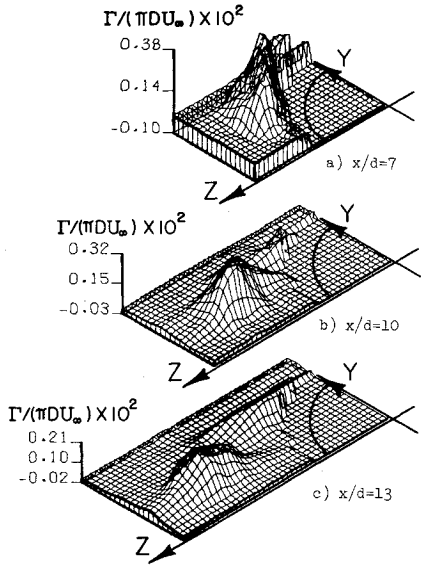

Fig. 4 Local circulation for $M_\infty = 1.95$, $R_d = 0.48 \times 10^6$, and $\alpha_b = 15$ deg.

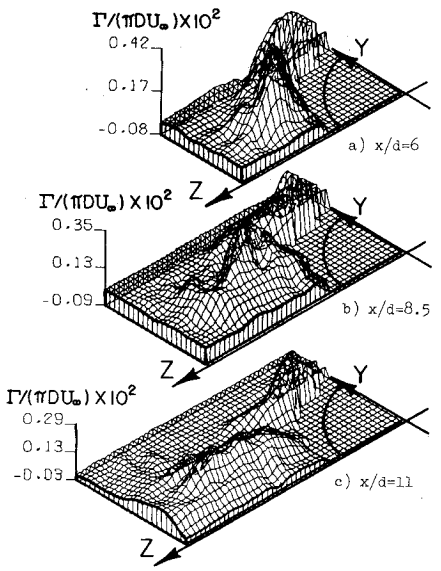

Fig. 5 Local circulation for $M_\infty = 1.95$, $R_d = 0.48 \times 10^6$, and $\alpha_b = 20$ deg.

this could be due to local convective acceleration of the vortex sheet near the vortex, that is, vortex line stretching.

Figure 5 shows a perspective plot of the local circulation for $\alpha_b = 20$ deg and $x/d = 6$, 8.5, and 11. At $x/d = 6$ (Fig. 5a) a stronger vortex exists compared to $\alpha_b = 15$ deg and $x/d = 7$ (Fig. 4a) but it is spread over a slightly larger region. Shortly after separation near the crest of the body, it is seen that the local vorticity increases along the sheet and then quickly decreases near the vortex core. At $x/d = 8.5$ and 11 (Figs. 5b and 5c) the vorticity is clearly seen to diffuse over a large region on the leeside. These plots quantitatively illustrate the "vortex cloud" suggested by vapor screen photographs of previous investigators (see, e.g., Jones and O'Hare[8] and Jorgensen[9]). At $\alpha_b = 25$ deg the same type of diffuse vorticity exists, except that it is even more diffused compared to the same body station for $\alpha_b = 20$ deg.

Another characteristic of the body vortex which was processed from the data was the approximate size of the vortex core. The size of the core was measured from plots of magnitude of cross-flow velocity vs radial coordinate in a

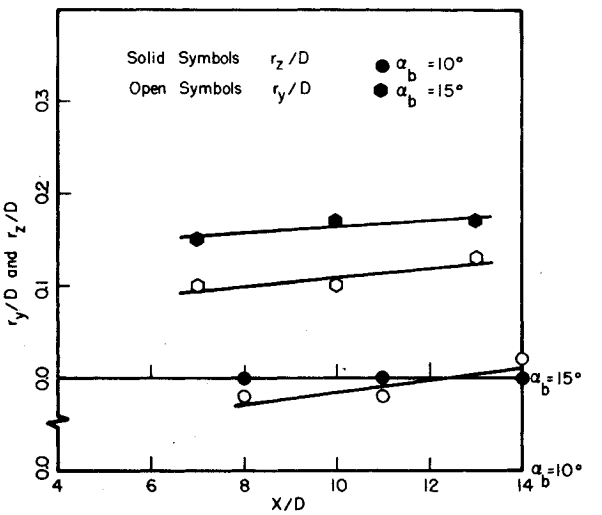

Fig. 6 Core radii for $M_\infty = 1.95$ and $R_d = 0.48 \times 10^6$.

vortex-oriented coordinate system. That is, an (r', ϕ) coordinate system was numerically constructed with the origin at the center of the vortex and the angular coordinate measured from the y body axis. Using this vortex-oriented coordinate system U_c/U_∞ vs r' could be plotted for various angles ϕ. Processing the data in this way showed that the body vortex cores tend to become elongated in the z direction as the angle of attack becomes large. Because of this elliptical characteristic two vortex core dimensions must be measured: a minor axis and a major axis. The angular orientation of these axes were determined such that the core radius of the minor axis r_y was the smallest and the core radius of the major axis r_z was the largest for all lines passing through the vortex center.

Figure 6 shows the vortex core radii vs x/d for $\alpha_b = 10$ and 15 deg. The vortex core radius, both the major and minor axes, is defined as the radial location (in a vortex coordinate system) at which $\partial U_c/\partial r' = 0$. Although this is a precise mathematical definition, plots of U_c/U_∞ vs r'/d required some interpretation in order to obtain the data shown in Fig. 6. For angles of attack larger than 15 deg the vortex core became so elongated in the streamwise direction that the core radii could not be measured with confidence. For the condition when a well-defined vortex does exist, the present data show that the solid body core is roughly 0.1-0.15 d. Figure 6 also shows that the core size grows very slowly with axial length.

Effect of Reynolds Number

In order to obtain a detailed understanding of the sensitivity of the body vortex wake to Reynolds number, the entire set of survey measurements was repeated for freestream conditions of $M_\infty = 2.00$ and $R_d = 1.75 \times 10^6$. This section will discuss comparisons between results for $R_d = 0.48 \times 10^6$ and 1.75×10^6 at $M_\infty = 2$. The survey grids, however, were not always the same size and shape as the low Reynolds number because the grids were changed during the experiment, as discussed in Sec. II, in order to best conform to the particular wake size.

Figure 7 shows the location of the vortex center in the cross-flow plane vs x/d for $\alpha_b = 10$, 15, 20, and 25 deg, $M_\infty = 2$, $R_d = 1.75 \times 10^6$. For $\alpha_b = 10$ deg it can be seen that the height of the vortex above the body is the same for both Reynolds numbers (Figs. 3a and 7a), but the vortex is positioned farther outboard for the high Reynolds number (Fig. 7b) as compared to the lower Reynolds number (Fig. 3b). For $\alpha_b \geq 15$ deg the y location of the vortex for both Reynolds numbers is identical, but the z coordinate shows significantly different trends with x/d for the two Reynolds numbers. For $\alpha_b \geq 15$ deg the high Reynolds number vortex is farther from the body for the low

x/d and closer to the body for large x/d. That is, the divergence angle between the vortex path and the body axis is lower at the high Reynolds number than at the low Reynolds number. This Reynolds number effect could have a significant impact on the forces and moments produced by the fins on a finned body of revolution. For fins of small span a change in vortex position of 0.2 d would produce, for example, sizable changes in force and moment variation with roll angle.

A perspective plot of the local circulation in the cross-flow plane for $\alpha_b = 20$ deg and $x/d = 6$, 8.5, and 11 is shown in Fig. 8. Comparing Fig. 8 with a similar plot for low Reynolds number (Fig. 5), one obtains an indication of the effects of Reynolds number. A qualitative comparison of $\Gamma(y,z)$ surfaces for the same x/d clearly shows the distinctive "roughness" of the high Reynolds number condition. At the high Reynolds number condition local flow disturbances, such as weak embedded waves, persist in the flow over longer axial distance as compared to the low Reynolds number. Comparing the forward body stations $x/d = 6$, for the low and high Reynolds numbers, one observes that the largest negative circulation in the grids is -0.08×10^{-2} and -0.22×10^{-2}, respectively. The large negative value for the high Reynolds number is due to a secondary separated flow region on the surface of the body. This secondary region lies underneath the vortex sheet, between the primary separation point on the side of the body and the secondary separation point on the leeward generator. The angular rotation in part of this separation bubble is clockwise thereby producing the large negative circulation shown in Fig. 8a. Several investigators have investigated this phenomenon, see, for example, Boersen[10] and Jorgensen.[9] One other feature noted in Fig. 8a is the extremely rapid drop in vorticity along the vortex sheet near the body. At $x/d = 8.5$ (Fig. 8b) the drop is not as pronounced and at $x/d = 11$ (Fig. 8c) it has essentially disappeared. This feature is not clearly understood. One possible suggestion is that the negative circulation of the separation bubble protrudes into the positive circulation of the vortex sheet from the primary separation, thereby canceling vorticity.

A novel means of qualitatively evaluating effects of Reynolds number is by comparing numerically generated streamline patterns. The stream function requires that the three-dimensional, incompressible, continuity equation, $\partial v/\partial y + \partial w/\partial z = -\partial u/\partial x$, be reduced to a two-dimensional form requiring $\partial u/\partial x = 0$. However, analysis of $\partial u/\partial x$ has shown that it is not approximately zero (see Ref. 4). As a result, the $\partial u/\partial x$ behaves as a source term in the cross-flow continuity equation. The magnitude of this term varied for different freestream conditions, but the largest values occurred at the forward body stations and then diminished along the body due to viscous dissipation. The case of $\alpha_b = 15$ deg and $x/d = 13$ was chosen because the $\partial u/\partial x$ was negligible throughout the survey region. Figure 9 shows streamline plots for $M_\infty \simeq 2$ and both Reynolds numbers. The streamlines were numerically generated from the nondimensionalized governing equation

$$\psi_B - \psi_A = \int_A^B (w/U_\infty)\,\mathrm{d}(y/d) - \int_A^B (v/U_\infty)\,\mathrm{d}(w/d)$$

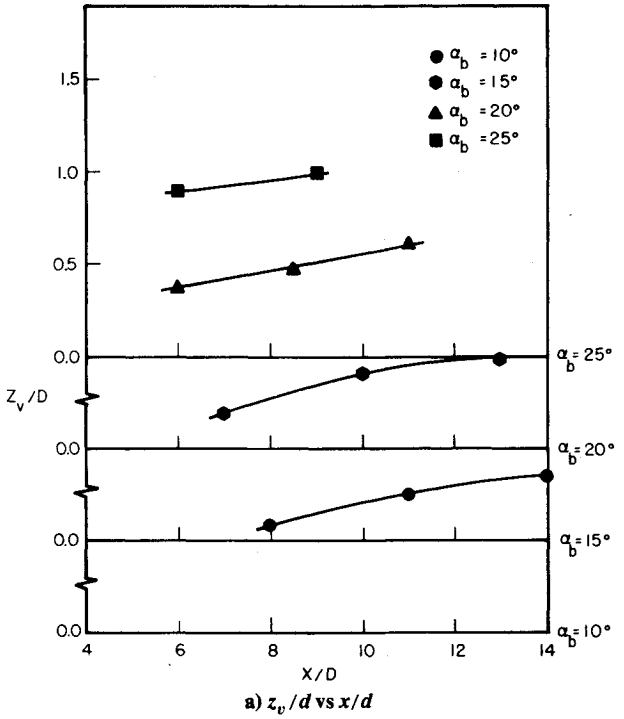

a) z_v/d vs x/d

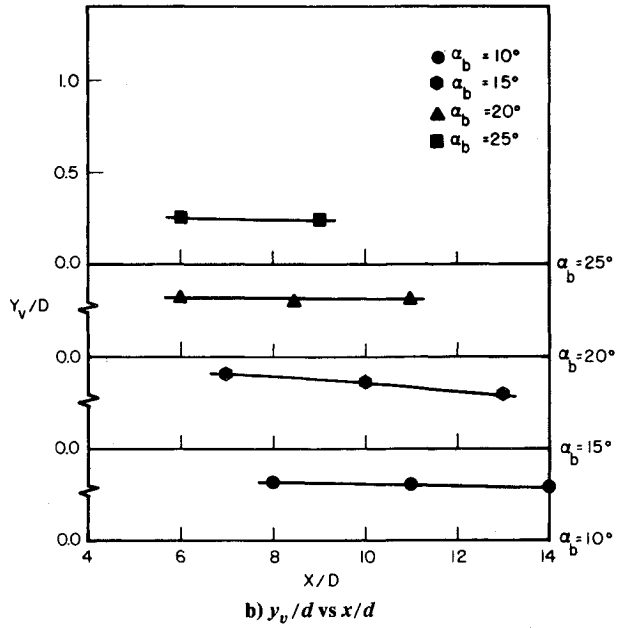

b) y_v/d vs x/d

Fig. 7 Vortex center location in cross-flow plane for $M_\infty = 2.00$ and $R_d = 1.75 \times 10^6$.

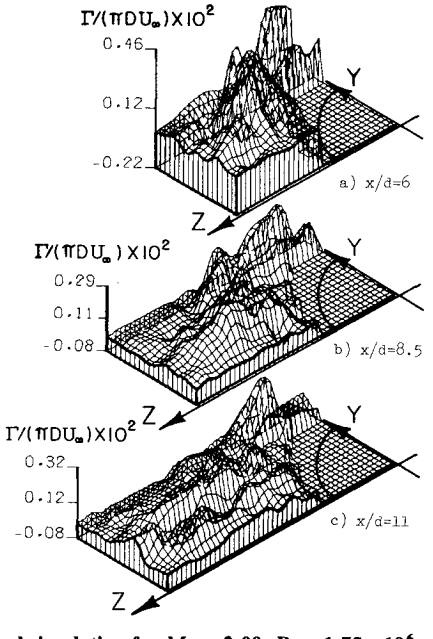

Fig. 8 Local circulation for $M_\infty = 2.00$, $R_d = 1.75 \times 10^6$, and $\alpha_b = 20$ deg.

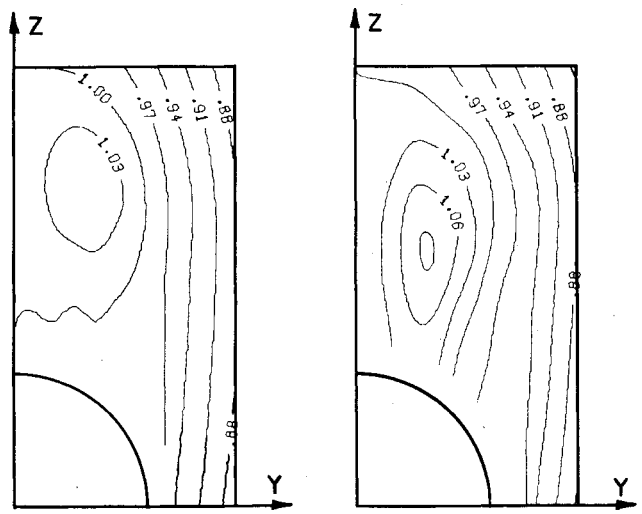

a) $M_\infty = 1.95$ and $R_d = 0.48 \times 10^6$ b) $M_\infty = 2.00$ and $R_d = 1.75 \times 10^6$

Fig. 9 Streamlines for $\alpha_b = 15$ deg and $x/d = 13$.

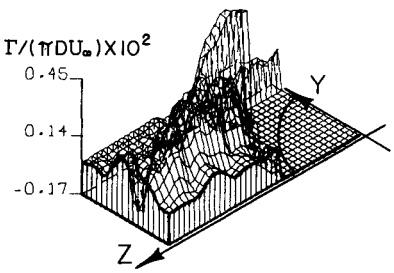

Fig. 10 Local circulation for $M_\infty = 2.00$, $R_d = 1.75 \times 10^6$, $\alpha_b = 25$ deg, and $x/d = 6$.

A cubic integration method, similar to the one used in circulation calculations discussed previously, was utilized. The numerical procedure was to arbitrarily set the streamline value at the top survey grid point on the centerline to unity and then calculate the line integrals by sweeping in the positive y and negative z directions. A comparison of the streamline contours in Fig. 9 clearly shows the elongation of the vortex with an increase in Reynolds number. This elliptical nature of the vortex core is similar to the angle-of-attack effects discussed earlier. The primary separation point for the low Reynolds number appears to be very near the crest of the body (Fig. 9a) whereas the separation point for the high Reynolds number appears to be farther downstream. The low Reynolds number condition should have laminar boundary-layer separation, with a cross-flow Reynolds number R_c of 0.12×10^6, and the high Reynolds number condition should exhibit turbulent separation, $R_c = 0.45 \times 10^6$.

At the high Reynolds number condition a very interesting feature of the vortex wake was pointed out in Ref. 4. This feature is a small secondary vortex located above the primary body vortex. It leaves the surface of the body near the nose and, consequently, it is referred to as a secondary nose vortex. Werlé[11] and Hsieh[12] obtained experimental evidence of the existence of such a vortex on blunt cylindrical bodies at high angles of attack. Hsieh suggests from his surface oil flow photographs that it rotates in the opposite direction of the primary body vortex. The present measurements confirm that this vortex exists, even on pointed bodies of revolution, and that it rotates in the opposite direction of the body vortex. Figure 10 shows the local circulation in the cross-flow plane for $\alpha_b = 25$ deg, for $x/d = 6$, $M_\infty = 2$ and $R_d = 1.75 \times 10^6$. The nose vortex appears as the small, negative circulation region near the top of the survey grid. Although the data show a spike of negative circulation, it is doubtful that the magnitude of the circulation is accurate because of the size of the vortex as compared to the probe.

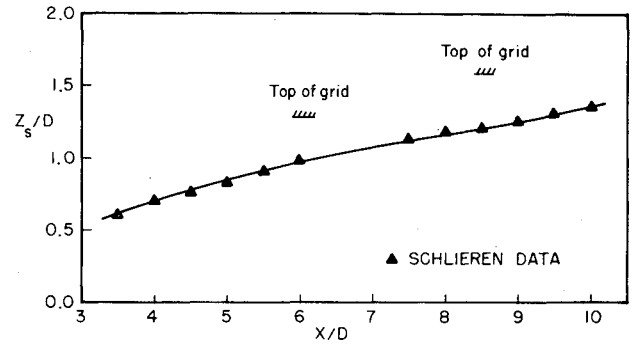

a) $\alpha_b = 20$ deg

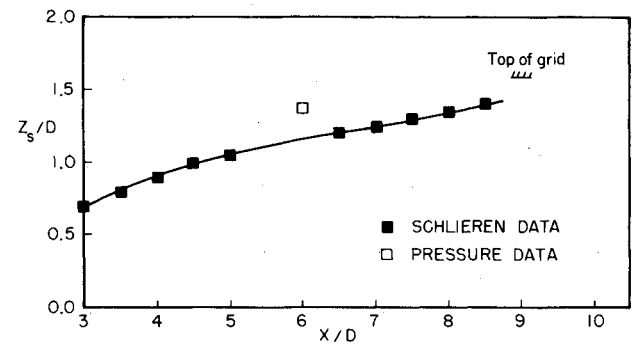

b) $\alpha_b = 25$ deg

Fig. 11 Nose vortex height in cross-flow plane for $M_\infty = 2.00$ and $R_d = 1.75 \times 10^6$.

Schlieren photograph measurements of this vortex were made because the secondary nose vortex was detected only on certain survey grids and because of questions concerning interference of the probe on the small vortex. The z coordinate of the secondary nose vortex z_s was measured from Schlieren photographs taken during the data acquisition for the survey grids. A comparison of these data with the survey data are shown in Fig. 11 for $\alpha_b = 20$ and 25 deg, $M_\infty = 2$, and $R_d = 1.75 \times 10^6$. The single data point for which the nose vortex was clearly detected in the survey regions is for $\alpha_b = 25$ deg, $x/d = 6$ (Fig. 11b). The agreement of the survey data point and the Schlieren data is poor. Also shown in Fig. 11 is the height of the individual survey grids. Comparing this with the nose vortex path from the Schlieren photographs clearly shows that it should have been detected on every grid for $\alpha_b = 20$ and 25 deg. Two possible reasons for errors exist in the survey data: first, the small nose vortex, roughly 0.1 d in diameter, passed between the survey grid points and, as a result, it was not detected; second, the large size of the probe compared to nose vortex caused the nose vortex to move or possibly burst. The Schlieren data in Fig. 11 were measured from several photographs of the same flowfield condition and are repeatable to within an error band of 0.05 d.

Effects of Mach Number

This section will discuss comparisons between results for $M_\infty = 2$ and $M_\infty = 3.01$ at $R_d \simeq 1.70 \times 10^6$. Figure 12 presents the location of the vortex center in the cross-flow plane vs x/d for $\alpha_b = 10$ and 15 deg, $M_\infty = 3.01$, $R_d = 1.70 \times 10^6$. Comparing the z coordinate of the vortex for $M_\infty = 3.01$ (Fig. 12a) with that for $M_\infty = 2$ (Fig. 7a) shows that they are practically identical; Mach number had no effect on the height of the body vortex in the wake. Comparing the y coordinates for the two Mach numbers reveals that for $\alpha_b = 10$ deg the y coordinates are identical, but for $\alpha_b = 15$ deg there is a slight difference. For $\alpha_b = 15$ deg the y coordinate remains constant for $M_\infty = 3.01$ while the y coordinate for $M_\infty = 2$ decreases slightly. For $\alpha_b = 20$ and 25 deg at $M_\infty = 3.01$ the vortex

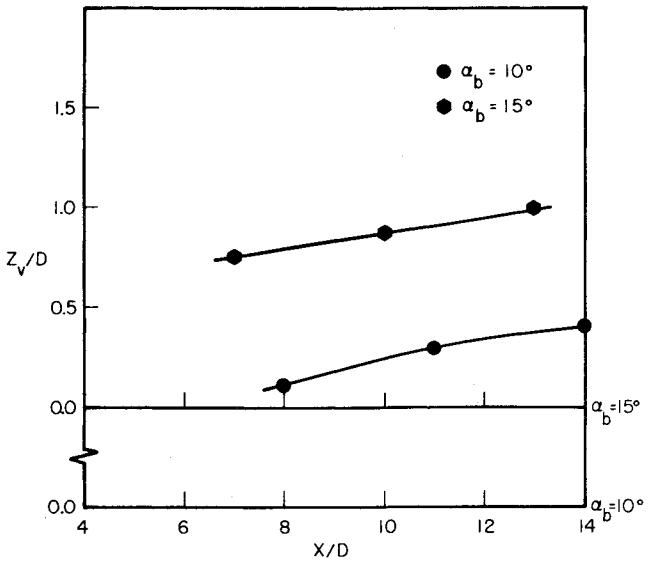

a) z_v/d vs x/d

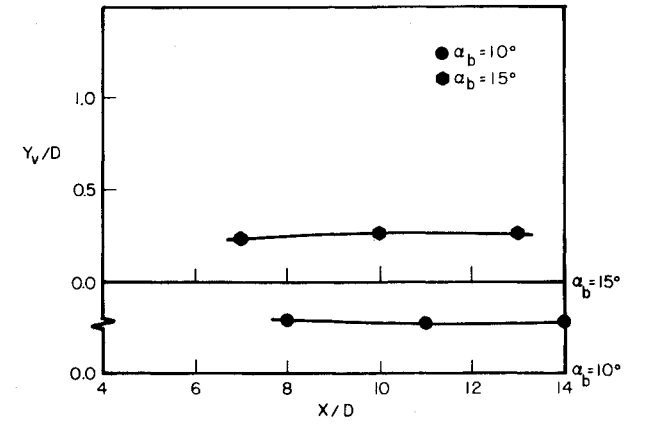

b) y_v/d vs x/d

Fig. 12 Vortex center location in cross-flow plane for $M_\infty = 3.01$ and $R_d = 1.70 \times 10^6$.

location could not be measured because a center could not be located on contour plots of p_0 and U_c. For $\alpha_b = 20$ and 25 deg at $M_\infty = 3.01$, a body vortex is essentially nonexistent. Contours of p_0 and U_c are not closed as one would expect for a vortex center but are nearly parallel lines extending from the crest of the body toward the downstream direction in the cross-flow plane.

Consider the effects of increasing M_∞ for a case where the body vortex still exists. Figure 13 shows numerically constructed streamlines for $\alpha_b = 15$ deg, $x/d = 13$, $M_\infty = 3.01$, and $R_d = 1.70 \times 10^6$. Comparing this figure to the corresponding figure for $M_\infty \simeq 2$ and $R_d = 1.75 \times 10^6$ (Fig. 9b) one obtains a graphic indication of the effects of compressibility in the cross-flow plane. The body vortex for $M_\infty \simeq 3$ is extremely elongated in the plane of symmetry. The vortex produces little distortion of the external flow for $M_\infty \simeq 3$, but simply provides a streamlining of the cylinder wake. The very slow rotational speed of the vortex for $M_\infty = 3$ as compared to $M_\infty = 2$ can be concluded from the difference in the number of streamlines enclosing each vortex.

A perspective plot of the local circulation distribution for $\alpha_b = 25$ deg, $x/d = 9$, and $M_\infty = 3.01$ is presented in Fig. 14. In order to visualize certain features of the wake more clearly, the perspective view in Fig. 14 is in the negative y, negative z direction and it is from a lower vantage point than the previous perspective plots. As mentioned earlier, a vortex is clearly not identifiable at this Mach 3 condition. The vortex

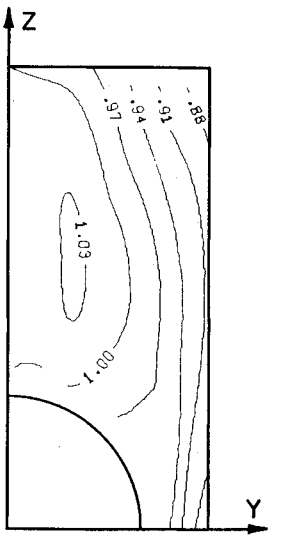

Fig. 13 Streamlines for $M_\infty = 3.01$, $R_d = 1.70 \times 10^6$, $\alpha_b = 15$ deg, and $x/d = 13$.

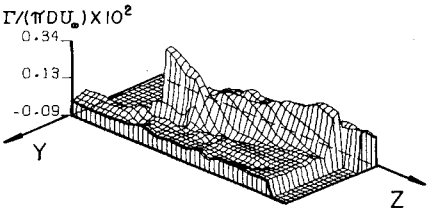

Fig. 14 Local circulation for $M_\infty = 3.01$, $R_d = 1.70 \times 10^6$, $\alpha_b = 25$ deg, and $x/d = 9$.

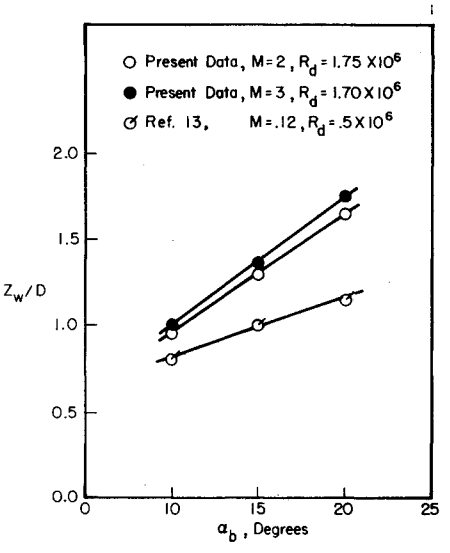

Fig. 15 Wake height in cross-flow plane for $x/d = 10$.

sheet leaving the crest of the body is still prominent, but the distribution does not show any concentrated cloud vorticity. The partial row of points at the top of the grid whose value is -0.09 are not measured data but a blanked plotting region, i.e., a data void region whose value is set at the lowest value in the grid. Upon careful examination one observes that almost all of the vorticity is contained in a ridge extending from the crest of the body toward the top corner of the survey grid near the z axis. This has the obvious characteristics of a shear layer wake similar to that of a circular cylinder perpendicular to a supersonic stream.

From the streamline plot (Fig. 13) and the perspective plot (Fig. 14) for Mach 3 one obtains the distinct impression that the height of the wake is substantially larger for Mach 3

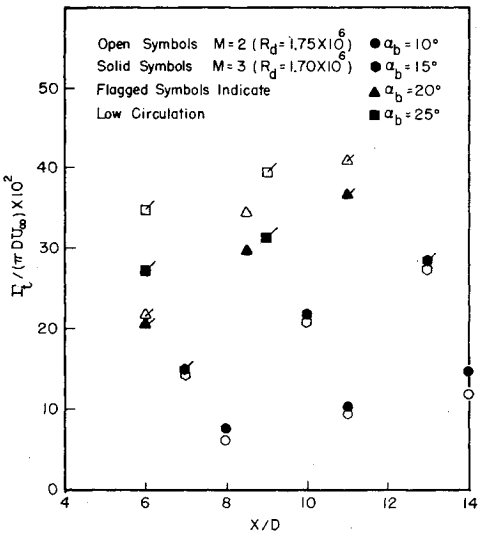

Fig. 16 Total circulation in the survey grids.

compared to Mach 2. A means of quantifying the wake height is shown in Fig. 15. The figure plots the attachment point on the z axis of the dividing streamline in the cross-flow plane vs angle of attack of the body for a ten-caliber long body. Present data for Mach 2 and Mach 3 are shown along with the incompressible flow data of Grosche.[13] As is clear from the figure, the change in wake height from Mach 2 to Mach 3 is minimal up to an α_b of 20 deg. The impression of a very long wake is simply due to the narrowing of the wake. Comparing the wake height of the present data to that of incompressible flow, the elongation of the wake due to cross-flow compressibility is demonstrated. Interpolating the data in Fig. 15 at an angle of attack of 20 deg permits one to conclude that significant compressibility effects already occur for a freestream Mach number of unity.

Figure 16 shows the relationship between the total circulation in the survey grid vs body length for $\alpha_b = 10$, 15, 20, and 25 deg, Mach 2 and Mach 3, $R_d \simeq 1.70 \times 10^6$. For $\alpha_b = 10$ and 15 deg a clearly linear variation of total circulation vs x is demonstrated. For $\alpha_b = 20$ and 25 deg, the variation is not as definite because many of the survey grids did not completely capture all of the circulation. That is, the flagged symbols in Fig. 16 denote that significant circulation passed through the top boundary of the grid. Consequently, the flagged symbols are a lower bound on the total circulation in the cross-flow plane. For $\alpha_b = 10$ and 15 deg it is seen that the Mach number change from 2 to 3 has little effect on total circulation in the field. For $\alpha_b = 20$ and 25 deg the data indicate that the Mach 2 wake contains significantly more circulation than the Mach 3 wake. This characteristic could be related to the change in the wake from a vortex cloud to a shear layer for Mach 2 and Mach 3, respectively. To obtain an indication of the relationship of total circulation to angle of attack of the body, a least squares fit of the data was calculated. Using the total circulation data for $x/d = 8$ and 11 and $\alpha_b = 10$, 15, and 20 deg, a fit of Γ_t vs $\sin^m \alpha_b$ was effected. The values of m for $M_\infty = 1.95$ and $R_d = 0.48 \times 10^6$, $M_\infty = 2.00$ and $R_d = 1.75 \times 10^6$, and $M_\infty = 3.01$ and $R_d = 1.70 \times 10^6$ were 2.82, 2.33, and 1.90, respectively. The correlation coefficients for the power fits were approximately 0.99, indicating that the plot of $\log \Gamma_t$ vs $\log \sin\alpha_b$ is very close to linear. The fit of the data demonstrates that the total circulation grows with angle of attack at a substantially lower rate as the Reynolds number and Mach number increases.

IV. Summary and Conclusions

1) The measured distribution of circulation in the cross-flow plane for Mach 2 shows that for $\alpha_b = 10$ and 15 deg and $x/d < 10$ the circulation is generally restricted to the vortex core and the vortex sheet. For $\alpha_b = 20$ and 25 deg the vorticity is diffused in the cross-flow plane to the extent that it could be described as a vortex cloud.

2) The present data for location of the body vortex in the cross-flow plane compare well with previous data of Jorgensen and Perkins[1] and Mello.[2] As these previous investigators used different pointed nose shapes than the present model, one can conclude that vortex position is not sensitive to this parameter.

3) The concentration of vorticity along the vortex feeding sheet is at a maximum near the body and then decreases near the vortex core. For certain cases, an extremely rapid decrease and then increase in sheet vorticity is observed near the body.

4) Measurements of an elliptic-shaped body vortex core are presented for $\alpha_b = 10$ and 15 deg. For $\alpha_b = 20$ and 25 deg the core is so elongated in the z direction that core dimensions cannot be defined.

5) For the high Reynolds number, Mach 2 condition, the body vortex does not move away from the body as rapidly as for the low Reynolds number condition.

6) The existence of a secondary nose vortex situated above the primary body vortex is confirmed. The secondary nose vortex rotates in the opposite direction as the body vortex.

7) The primary body vortex position in the cross-flow plane was measured for $M_\infty = 3$ at $\alpha_b = 10$ and 15 deg. For $\alpha_b = 20$ and 25 deg cross-flow compressibility distorts the body vortex to an extent that a body vortex cannot be defined. Local circulation in the cross-flow plane for $\alpha_b = 20$ and 25 deg shows that the vorticity is primarily located in a shear layer originating near the crest of the body and extending downstream.

8) Although the wake is distorted due to compressibility, the wake height for Mach 2 and 3 are roughly the same for $\alpha_b \leq 20$ deg.

9) The total circulation in the wake for $\alpha_b \leq 15$ deg did not change between Mach 2 and Mach 3. For $\alpha_b = 25$ deg the measurements indicate that the Mach 2 wake contains significantly more circulation than the Mach 3 wake.

Acknowledgments

The authors would like to thank Donald C. Daniel, Aerodynamics Research Manager, of the Air Force Armament Laboratory for his comments and suggestions during the investigation. We also thank the Project Engineers for our experiment, Bill Martindale and Terry Penny, ARO, Inc., AEDC, for their efforts. The work was supported by the Air Force Armament Laboratory, Eglin AFB, Fla., under AF Contract F08635-77-C-0049.

References

[1] Jorgensen, L. H. and Perkins, E. W., "Investigation of Some Wake Vortex Characteristics of an Inclined Ogive-Cylinder Body at Mach No. 2," NACA Rept. 1371, May 1955.

[2] Mello, J. F., "Investigation of Normal Force Distributions and Wake Vortex Characteristics of Bodies of Revolution at Supersonic Speeds," *Journal of the Aerospace Sciences*, Vol. 26, March 1959, pp. 155-168.

[3] Thomson, K. D. and Morrison, D. F., "The Spacing, Position and Strength of Vortices in the Wake of Slender Cylindrical Bodies at Large Incidence," *Journal of Fluid Mechanics*, Vol. 50, Pt. 4, 1971, pp. 751-783.

[4] Oberkampf, W. L., Bartel, T. J., and Martindale, W. R., "Supersonic Flow Measurements in the Body Vortex Wake of an Ogive Nose Cylinder," AIAA Paper 78-787, San Diego, Calif., April 19-21, 1978.

[5] Oberkampf, W. L., and Bartel, T. J., "Supersonic Flow Measurements in the Body Vortex Wake of an Ogive Nose Cylinder," Air Force Armament Laboratory Rept., Eglin AFB, Fla., AFATL-TR-78-127, Nov. 1978.

[6] Oberkampf, W. L. and Nicolaides, J. D., "Aerodynamics of Finned Missiles at High Angle of Attack," *AIAA Journal*, Vol. 9, Dec. 1971, pp. 2378-2384.

[7]Oberkampf, W. L., "Prediction of Roll Moments on Finned Bodies in Supersonic Flow," *Journal of Spacecraft and Rockets*, Vol. 12, Jan. 1975, pp. 17-21.

[8]Jones, J. H. and O'Hare, J. E., "Flow Visualization Photographs of a Yawed Tangent Ogive Cylinder at Mach Number 2," Arnold Engineering Development Center, AEDC-TR-73-45, March 1973.

[9]Jorgensen, L. H., "Prediction of Static Aerodynamic Characteristics for Slender Bodies Alone and with Lifting Surfaces to Very High Angles of Attack," NASA TR-R-474, Sept. 1977.

[10]Boersen, S. J., "Reynolds Number Effects on Pressure and Normal Force Distributions Along Conically Pointed Circular Cylinder at Freestream Mach Number 2.3," National Aerospace Laboratory, NLR Rept. NLR-TR-75124-U, The Netherlands, 1975.

[11]Werlé, H., "Separation on Axisymmetrical Bodies at Low Speed," *La Recherche Aéronautique*, No. 90, Sept.-Oct. 1962.

[12]Hsieh, T., "An Investigation of Separated Flows About a Hemisphere-Cylinder at Incidence in the Mach Number Range from 0.6 to 1.5," AIAA Paper 77-179, Los Angeles, Calif., Jan. 1977.

[13]Grosche, F. R., "Wind Tunnel Investigation of the Vortex System Near an Inclined Body of Revolution With and Without Wings," *Aerodynamic Interference*, AGARD-CP-71-71, Jan. 1971.